

Physics-Consistent Diffusion for Efficient Fluid Super-Resolution via Multiscale Residual Correction

Zhihao Li¹ Shengwei Dong⁴ Chuang Yi⁴ Junxuan Gao⁴ Zhilu Lai^{1,2}
 Zhiqiang Liu^{3*} Wei Wang^{1,2*} Guangtao Zhang^{3,4*}

¹The Hong Kong University of Science and Technology (Guangzhou), Guangzhou, China

²The Hong Kong University of Science and Technology, Hong Kong SAR, China

³Southern University of Science and Technology, Shenzhen, China

⁴SandGold AI Research, Guangzhou, China

zli416@connect.hkust-gz.edu.cn; liuzq@sustech.edu.cn; weiwcs@ust.hk; tao@sgd-ai.com

Abstract

*Existing image SR and generic diffusion models transfer poorly to fluid SR: they are sampling-intensive, ignore physical constraints, and often yield spectral mismatch and spurious divergence. We address fluid super-resolution (SR) with **ReMD** (Residual-Multigrid Diffusion), a physics-consistent diffusion framework. At each reverse step, ReMD performs a multigrid residual correction: the update direction is obtained by coupling data consistency with lightweight physics cues and then correcting the residual across scales; the multiscale hierarchy is instantiated with a multi-wavelet basis to capture both large structures and fine vortical details. This coarse-to-fine design accelerates convergence and preserves fine structures while remaining equation-free. Across atmospheric and oceanic benchmarks, ReMD improves accuracy and spectral fidelity, reduces divergence, and reaches comparable quality with markedly fewer sampling steps than diffusion baselines. Our results show that enforcing physics consistency inside the diffusion process via multigrid residual correction and multi-wavelet multiscale modeling is an effective route to efficient fluid SR. Our code are available on <https://github.com/lizhihao2022/ReMD>.*

1. Introduction

High-resolution (HR) fluid fields are crucial for understanding transport, extremes, and subgrid-scale variability in climate and computational fluid dynamics (CFD). However, operational systems typically run at coarse resolution to satisfy wall-time and cost constraints. Running full-physics solvers or learned surrogates at HR remains one to two or-

ders of magnitude more expensive than at low resolution. As a result, a practical pipeline has emerged: first obtain a coarse solution using a numerical model or a neural operator [10, 12], then apply a learned super-resolution (SR) model to reconstruct HR details [17, 20, 23].

Directly applying generic image SR to fluid SR is problematic. Geophysical and turbulent flows have wide-band, multiscale spectra and filamentary structures whose statistics differ from natural images; pixel/feature losses on RGB data tend to distort both low- and high-frequency content, yielding incorrect energy spectra and missing small eddies. Standard SR models also lack physics consistency—often introducing spurious divergence, violating simple flux/boundary behavior, and degrading stability under rollout [1, 9]. Finally, one-shot LR to HR mappings underuse the fact that a coarse solution u_0 already approximates the target operator, overlooking the benefits of iterative residual correction familiar from multigrid.

Diffusion models are appealing here because they refine solutions iteratively and can impose strong generative priors for fine structures [18, 19]. However, off-the-shelf diffusion for images is ill-matched to fluid SR: the forward process injects pure noise that drifts away from coarse/physical manifolds, the reverse updates are typically oblivious to physics and spectra, and many sampling steps inflate cost. Our approach addresses these gaps by placing a multiscale, physics-aware residual correction *inside* the reverse process. A preview in Fig. 1 shows that, given the same LR initial solution, **ReMD** reconstructs sharper vortical structures and yields substantially lower error maps than diffusion and non-diffusion baselines, using only 5 reverse steps versus 15 for ResShift.

We instead view fluid SR as *iterative residual correction* on top of a given coarse solution, in the spirit of multigrid methods [2, 6, 13]. At each reverse step, we want to mea-

*Corresponding author.

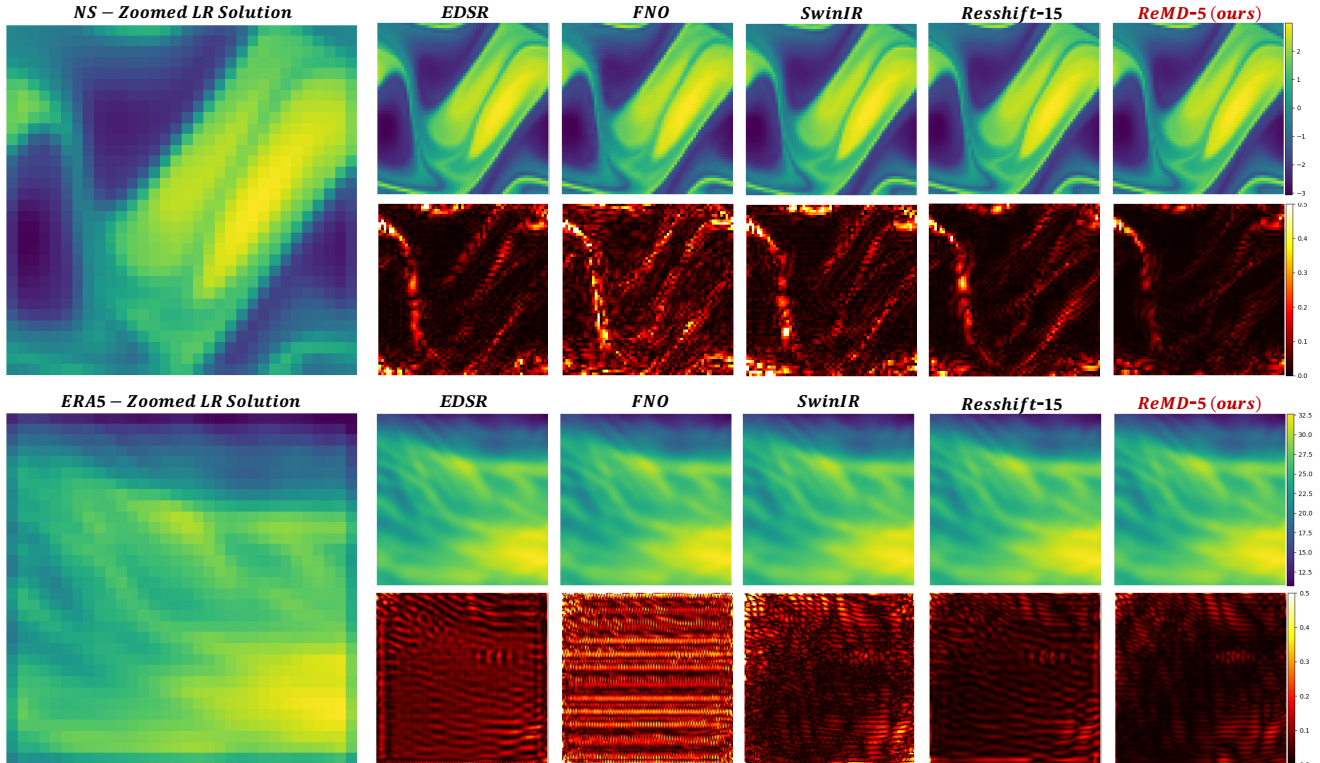


Figure 1. **Qualitative comparison on NS ($\times 2$) and ERA5 ($\times 4$).** Each block shows (left) a zoomed LR input u_0 , (top row) HR reconstructions, and (bottom row) absolute error maps w.r.t. ground truth (shared color scale per block). With only **5** reverse steps, **ReMD** yields (NS) sharper filaments/coherent fronts and (ERA5) preserved mesoscale shear bands while suppressing ringing/stripe artifacts seen in EDSR/FNO/SwinIR, and achieves lower errors than *ResShift* despite requiring **5** vs. **15** steps.

sure how inconsistent the current HR estimate u_t is with the available low-resolution information and with lightweight physics cues, and then correct this residual across scales. This connects to residual-based diffusion such as ResShift [25], which samples in a residual space rather than directly in image space. Our formulation is similar in spirit but differs in three key aspects. (i) The residual is *recomputed at every step* from a data-consistency term and an equation-free physics residual, rather than being a fixed HR–LR difference. (ii) The correction is performed by a *multiscale* operator derived from multigrid and multiwavelet ideas. (iii) The design is tailored to fluid fields: it operates on scalar/vector components, respects simple physical structure (e.g., divergence, masks, spectra), and can be used on top of coarse solutions produced by either classical solvers or neural operators.

Building on this view, we introduce **ReMD** (*Residual–Multigrid Diffusion*), a physics-consistent diffusion framework for fluid SR. **ReMD** realized an operator from the coarse space to HR with few, coarse-to-fine steps, improving spectral fidelity and reducing spurious divergence. Our main contributions are:

- **Formulation.** We cast fluid SR as operator learning via

few-step *residual* diffusion: instead of direct denoising, ReMD iteratively corrects a coarse solution with physics-consistent updates.

- **Multiscale drift.** We embed a time-gated multi-grid V-cycle (multiwavelet restriction/prolongation with lightweight learned smoothers) as the per-step drift inside the sampler, yielding stable coarse-to-fine corrections.
- **Equation-free physics.** We design fully differentiable, inexpensive physics residuals (e.g., divergence, spectrum alignment) that require no PDE at test time.
- **Effectiveness and efficiency.** Across NS, ERA5, and Ocean benchmarks, ReMD attains higher accuracy and spectral fidelity with lower divergence than diffusion and non-diffusion baselines, while matching or exceeding their quality with markedly fewer sampling steps.

2. Preliminaries

In this section, we formalize fluid super-resolution as an operator-learning map from coarse fields to high-resolution states and fix the notation used throughout (§2.1). We then recall the classical multigrid residual-correction principle, which later serves as the time-conditioned corrector inside

our diffusion refinement (§2.2).

2.1. Problem formulation

We cast fluid SR as *operator learning* between function spaces. Let \mathcal{U} be the HR state space (e.g., scalar/vector fields on a spatial domain) and \mathcal{U}_c its coarse counterpart. Given a coarse field $u^{\text{LR}} \in \mathcal{U}_c$, we seek to reconstruct the unknown HR field $u^{\text{HR}} \in \mathcal{U}$ by learning

$$\mathcal{F}_\theta : \mathcal{U}_c \rightarrow \mathcal{U}, \quad \hat{u}^{\text{HR}} = \mathcal{F}_\theta(u^{\text{LR}}). \quad (1)$$

Restriction consistency. We assume a known restriction operator $R : \mathcal{U} \rightarrow \mathcal{U}_c$ (e.g., averaging/downsampling) and aim for coarse-scale consistency $R(\hat{u}^{\text{HR}}) \approx u^{\text{LR}}$. We do *not* assume access to governing equations or to the true solution operator; u^{LR} may come from any upstream pipeline, and R provides a common coarse-space reference.

Iterative diffusion SR. We realize \mathcal{F}_θ as a finite reverse-time refinement. Let u_t be the HR estimate at step t ($t = T, \dots, 1, 0$). We update

$$u_{t-1} = u_t + \alpha_t e_t + \sigma_t \varepsilon_t, \quad \varepsilon_t \sim \mathcal{N}(0, \mathbf{I}), \quad (2)$$

with schedules α_t, σ_t . Define the residual and the time-conditioned corrector by

$$r(u) = u^{\text{LR}} - R(u), \quad e_t = S_t(r(u_t)),$$

where S_t is the residual corrector with timestep gating. Thus,

$$\mathcal{F}_\theta : u^{\text{LR}} \mapsto u_T \mapsto \dots \mapsto u_0 \equiv \hat{u}^{\text{HR}}.$$

2.2. Residual correction via multigrid

Multigrid (MG) [2, 24] accelerates iterative solvers by letting each scale remove the errors it sees best: smooth (low-frequency) errors on coarse grids and oscillatory (high-frequency) errors on fine grids. Consider a linear system on a fine grid Ω^h ,

$$A^h u^h = b^h, \quad (3)$$

with linear restriction I_h^{2h} and prolongation I_{2h}^h between Ω^h and Ω^{2h} . Let $u^{h,(k)}$ be the current fine-grid iterate (iteration index k). A two-level V-cycle that maps $u^{h,(k)} \mapsto u^{h,(k+1)}$ proceeds as:

1) Pre-smoothing. Damp high-frequency error on the fine grid:

$$\tilde{u}^{h,(k)} \leftarrow \text{Smooth}^h(u^{h,(k)}, A^h, b^h). \quad (4)$$

2) Residual transfer. Form the fine-grid residual and restrict it to the coarse grid:

$$r^{h,(k)} = b^h - A^h \tilde{u}^{h,(k)}, \quad r^{2h,(k)} = I_h^{2h} r^{h,(k)}. \quad (5)$$

3) Coarse correction. Approximately solve the coarse error equation:

$$A^{2h} e^{2h,(k)} = r^{2h,(k)}. \quad (6)$$

4) Prolongation and update. Lift the coarse error and correct the fine-grid state:

$$\hat{u}^{h,(k)} \leftarrow \tilde{u}^{h,(k)} + I_{2h}^h e^{2h,(k)}. \quad (7)$$

5) Post-smoothing. Remove high-frequency components reintroduced by prolongation and obtain the next iterate:

$$u^{h,(k+1)} \leftarrow \text{Smooth}^h(\hat{u}^{h,(k)}, A^h, b^h). \quad (8)$$

One V-cycle thus defines an iterative mapping $u^{h,(k+1)} = \text{V-cycle}(u^{h,(k)})$. Later, we reuse this classical “residual \rightarrow restrict \rightarrow coarse correction \rightarrow prolong \rightarrow smooth” principle as a time-conditioned residual corrector S_t for constructing the update direction e_t in the iterative diffusion refinement (where the role of $u^{h,(k)}$ is played by the current HR estimate u_t).

3. Methodology

Building on the operator view in Sec. 2, we instantiate **ReMD** as a few-step diffusion sampler in which *each reverse step performs a multiscale residual correction*. Concretely, at every step we (i) form a residual that enforces coarse-scale consistency and lightweight physics cues, (ii) transport that residual across resolutions with a time-gated multigrid pass using *fixed* multiwavelet restriction/prolongation, and (iii) apply a small learned head to make a minor refinement.

The sampler composition is described in Sec. 3.1; the time-gated multigrid corrector and its multiwavelet transfers are detailed in Sec. 3.2; the lightweight, equation-free physics cues are specified in Sec. 3.3; and training choices and schedules are summarized in Sec. 3.4. Fig. 2 provides a high-level overview of the residual formation, multiscale correction, and reverse update.

3.1. Sampler with multiscale residual drift

Let u_t be the HR estimate at reverse step t ($t = T, \dots, 1, 0$). We update

$$u_{t-1} = u_t + \alpha_t e_t + \beta_t g_\theta(u_t, t) + \sigma_t \varepsilon_t, \quad \varepsilon_t \sim \mathcal{N}(0, I), \quad (9)$$

where g_θ is a small learned head (zero-initialized last layer), and $\alpha_t, \beta_t, \sigma_t$ are schedules (DDIM when $\sigma_t=0$). The drift direction e_t is obtained from a *time-conditioned residual corrector*

$$r(u) = u^{\text{LR}} - R(u) + \lambda(t) \rho(u), \quad e_t = S_t(r(u_t)), \quad (10)$$

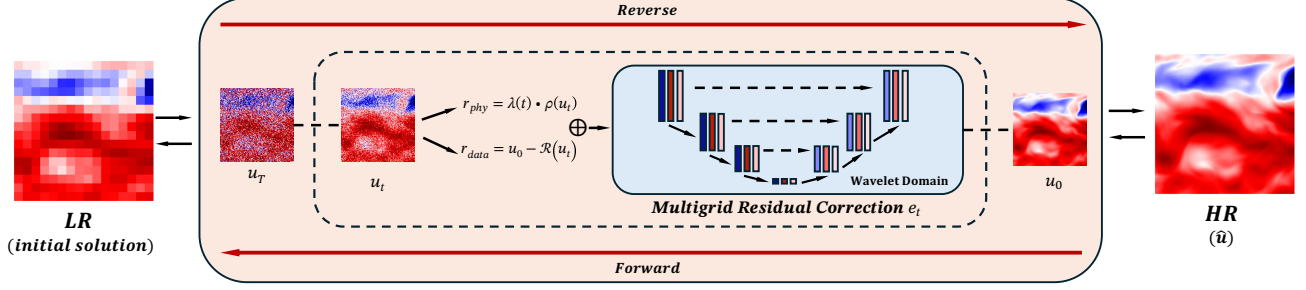


Figure 2. Overview of ReMD. Starting from a coarse LR initial solution, the reverse diffusion steps refine the HR estimate u_t while a multigrid residual correction module combines data-consistency and physics residuals in the wavelet domain, yielding the final HR field \hat{u} .

with known restriction R (e.g., averaging/downsampling), lightweight physics cues $\rho(\cdot)$ (Sec. 3.3), and a time-gated MG corrector S_t (Sec. 3.2).

3.2. Time-gated multigrid residual corrector

The corrector S_t implements the classical “residual \rightarrow restrict \rightarrow coarse correction \rightarrow prolong \rightarrow smooth” principle in a learnable, *time-gated* form:

$$S_t(r) = \text{Smooth}_0(r) + \sum_{\ell=1}^L w_\ell(t) P_\ell \text{Smooth}_\ell(R_\ell r), \quad (11)$$

where R_ℓ, P_ℓ are fixed multiwavelet restriction/prolongation operators, Smooth_ℓ are small conv smoothers, and gates $w_\ell(t) \in (0, 1)$ come from a timestep embedding followed by a tiny MLP and sigmoid. Early steps emphasize coarse levels (removing low-frequency errors); later steps emphasize fine levels (refining sharp fronts). Because transfers are fixed and depthwise-separable smoothers are used, the per-step complexity is $\mathcal{O}(HW)$ per level with a small constant.

Multiwavelet mapping operators. Inspired by M2NO [13], we implement the multigrid residual corrector with *fixed multiwavelet transfers* so that restriction/prolongation are spectrally clean and parameter-free, while only within-level smoothers are learned. Let H_x, H_y be 1D low-pass (scaling) filters from an orthonormal multiwavelet system; in 2D we use separable tensors

$$R \equiv I_h^{2h} = H_y \otimes H_x, \quad P \equiv I_{2h}^h = R^\top, \quad (12)$$

where \otimes is the Kronecker product. On a hierarchy, level-wise filters R_ℓ, P_ℓ are obtained by dyadic dilation/shift of the base filters; we keep them *fixed*. This yields stable, $\mathcal{O}(HW)$ inter-level mappings with sharp low/high-frequency separation, while the learned smoothers are tiny depthwise 3×3 convolutions gated by the timestep.

Intuitively, coarse levels remove large-scale bias early; fine levels sharpen fronts/vortices later. Because R_ℓ, P_ℓ are fixed and smoothers are depthwise, the per-step cost stays close to standard CNN diffusion.

3.3. Physics-consistent residuals

We regularize the reverse updates with lightweight, differentiable *physics-consistent residuals* that operate on a *single* scalar field (e.g., u, u_x, v_x , temperature). Each residual returns a pixel-space direction with the same shape as the input and is fully backpropagable. Let $u \in \mathbb{R}^{1 \times H \times W}$ be the target field at step t , u_0 its coarse/anchor field, and $M \in \{0, 1\}^{1 \times H \times W}$ an optional fluid mask (1=fluid). We write the total physics residual as

$$\rho(u) = \sum_k w_k \rho_k(u; u_0, M), \quad (13)$$

where $r_{\text{data}}(u)$ is the data-consistency residual (e.g., $u_0 - R(u)$), w_k are fixed weights, and $\lambda(t)$ is a schedule.

(1) Laplacian / Biharmonic smoothing. To suppress spurious oscillations while preserving large scales, we use the negative gradients of quadratic smoothness energies:

$$\rho_{\text{lap}}(u) = -\Delta u, \quad \rho_{\text{bi}}(u) = -\Delta(\Delta u), \quad (14)$$

implemented with small-depthwise convolutions (stable and fast). ρ_{bi} more aggressively removes checkerboard/ringing artifacts and is useful for derivative fields such as u_x .

(2) Anisotropic edge-preserving diffusion. We protect sharp fronts/filaments using a Perona–Malik style flux guided by an anchor (coarse) field u_a (default $u_a = u_0$):

$$\rho_{\text{aniso}}(u) = -\nabla \cdot \left(g(\|\nabla u_a\|) \nabla u \right), \quad g(s) = \frac{1}{1 + (s/\kappa)^2}. \quad (15)$$

Early steps emphasize coarse guidance; later steps are relaxed via time gating inside ρ_{aniso} .

(3) Spectrum alignment. We match the radial log-power spectrum of u to an anchor (e.g., u_0) to enforce realistic

Table 1. **Quantitative comparison on three fluid SR benchmarks.** NS (2×), ERA5 (4×), and Ocean (4×). We report RMSE↓, PSNR↑, and SSIM↑. **Bold** denotes the best and underline the second-best within each dataset/metric block. **ReMD** attains the lowest errors and top (or tied) perceptual scores across datasets while using only 2–5 reverse steps, compared with 15 steps for the ResShift baseline.

| MODEL | NS | | | ERA5 | | | OCEAN | | |
|---------------|-----------------|--------------|--------------|-----------------|--------------|--------------|-----------------|--------------|--------------|
| | RMSE ↓ | PSNR ↑ | SSIM ↑ | RMSE ↓ | PSNR ↑ | SSIM ↑ | RMSE ↓ | PSNR ↑ | SSIM ↑ |
| EDSR | 2.97E-02 | 46.89 | 0.996 | 9.06E-02 | 57.13 | <u>0.998</u> | 1.36E-02 | 47.48 | <u>0.982</u> |
| FNO | 4.42E-02 | 43.44 | 0.988 | 1.35E-01 | 53.69 | 0.997 | 1.67E-02 | 45.74 | 0.974 |
| MWT | 8.45E-02 | 37.81 | 0.970 | 6.13E-01 | 40.53 | 0.968 | 4.55E-02 | 37.03 | 0.852 |
| HiNOTE | 8.03E-02 | 38.25 | 0.973 | 2.12E-01 | 49.76 | 0.994 | 1.99E-02 | 44.21 | 0.964 |
| GALERKIN | 5.32E-02 | 41.83 | 0.981 | 3.45E-01 | 45.51 | 0.988 | 3.75E-02 | 38.70 | 0.890 |
| SWINIR | 3.63E-02 | 45.15 | 0.994 | 9.10E-02 | 57.09 | <u>0.998</u> | 1.35E-02 | 47.55 | 0.983 |
| SR3 | 3.34E-01 | 25.87 | 0.841 | 7.13E+00 | 17.37 | 0.762 | 7.86E-02 | 32.27 | 0.888 |
| RESSHIFT-15 | 2.21E-02 | 49.47 | <u>0.997</u> | 8.79E-02 | 57.39 | <u>0.998</u> | 1.36E-02 | 47.50 | 0.981 |
| REMD-2 | <u>2.11E-02</u> | 49.84 | 0.998 | <u>8.03E-02</u> | <u>58.13</u> | 0.999 | 1.32E-02 | 47.72 | 0.983 |
| REMD-5 | 2.09E-02 | 49.94 | 0.998 | 8.02E-02 | 58.19 | 0.999 | <u>1.33E-02</u> | <u>47.71</u> | 0.983 |

spectral slopes while remaining equation-free. Let \mathcal{F} be the FFT and \mathcal{B} the inverse FFT. With bin-wise weights $W(k)$ derived from binned log-power discrepancies,

$$\rho_{\text{spec}}(u) = \mathcal{B}(W(k) \odot \mathcal{F}(u)), \quad (16)$$

where $W(k)$ uses a robust (Huber) transform of $\log P(u)$ minus the target log-power. Optional masking reduces coastline-induced ringing.

We combine the above residuals as in Eq. (13). Each term is implemented via depthwise convolutions or FFT/iFFT, thus fully differentiable and efficient ($\mathcal{O}(HW)$ per pass). A cosine $\lambda(t)$ emphasizes physics early and decays moderately later, while fine-grained time gating inside individual ρ_k (e.g., in ρ_{aniso}) produces a coarse-to-fine prior that complements the multiscale residual correction in the reverse process.

3.4. Training objective and schedules

We adopt standard diffusion training with an ε -prediction loss and a cosine noise schedule; the MG drift is used in the reverse mean during training and inference via Eq. (9)–(10). Given forward-diffused pairs (u_t, ε) ,

$$\mathcal{L}(\theta) = \mathbb{E}_{t, u_t, \varepsilon} \left[\|\varepsilon - \hat{\varepsilon}_\theta(u_t, t)\|_2^2 \right], \quad (17)$$

and we instantiate the reverse mean as

$$\mu_\theta(u_t, t) = u_t + \alpha_t e_t + \beta_t g_\theta(u_t, t), \quad e_t = S_t(r(u_t)).$$

At test time, we use DDIM ($\sigma_t=0$) with 5–10 NFEs; by keeping the trajectory close to the restriction/physics manifold, ReMD attains target quality with markedly fewer steps than vanilla diffusion.

4. Experiments

In this section we evaluate **ReMD** under a unified protocol: we outline datasets, training and metrics, then report main results with representative visual comparisons. We further probe behaviour via frequency–domain analysis, patch-level spatial inspection, and ablations that isolate the roles of multigrid correction and physics cues, followed by brief discussion of design implications.

4.1. Experimental Setup

Testing Datasets. We evaluate on three benchmarks: Navier–Stokes (NS) flows from PDEBench [21], ERA5 reanalysis [7], and the Global Ocean Surface Velocity dataset [4]. The SR settings are fixed per dataset: **NS** uses 2× SR; **ERA5** and **Ocean** use 4× SR. For ERA5 and Ocean we extract HR patches of 256×256 via sliding windows; the corresponding LR inputs are generated by applying the RealESRGAN degradation operator [22] with the prescribed scale. NS follows the dataset’s native grid and the same degradation protocol for the 2× setting.

Training Details. Unless noted otherwise, we train a single ReMD model per dataset/scale using Adam [8] (PyTorch [16]) with batch size 64, learning rate 5×10^{-5} , and $\sim 100k$ iterations. LR–HR pairs are formed using the RealESRGAN degradation at the corresponding scale (2× for NS; 4× for ERA5/Ocean). Additional dataset statistics and preprocessing details are provided in the appendix.

Compared Methods. We evaluate the effectiveness of ReMD in comparison to nine recent methods, including two diffusion-based models, SR3 [26] and ResShift [25], one CNN-based method, EDSR [11], two transformer-based

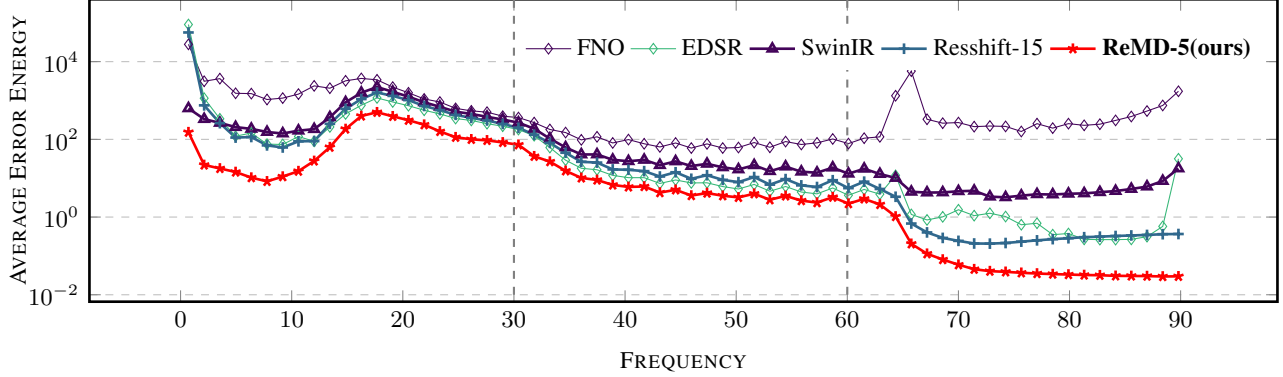


Figure 3. **Error–energy spectrum on ERA5 ($\times 4$).** Radial average of the Fourier-domain error (log scale on y) versus frequency (x). Vertical dashed lines mark the LR Nyquist band and the transition toward the HR band. **ReMD-5** (red) maintains the lowest error from large to high scales, remaining below *ResShift-15*, FNO and image-SR baselines (EDSR, SwinIR), indicating superior spectral fidelity.

methods, SwinIR [14] and Galerkin Transformer [3], as well as three established operator learning methods, namely Fourier Neural Operator (FNO) [12], Multiwavelet Transform (MWT) [5], and HiNOTE [15].

Metrics. We report **RMSE** (primary), **PSNR**, and **SSIM**. To evaluate *physics-related proxies*, we additionally report (i) **VE/EE** on NS2D and (ii) **GED** on ERA5_uo, and we analyze **radial spectra** (energy / error-energy) to quantify frequency fidelity. These proxies provide lightweight diagnostics of physically plausible structure, but they do *not* guarantee satisfaction of the governing PDE.

4.2. Experimental Results

We evaluate on three settings, each with a single upscaling factor: **NS** ($2\times$), **ERA5** ($4\times$), and **Ocean** ($4\times$). Tab. 1 reports RMSE/PSNR/SSIM; Fig. 1 provides qualitative comparisons (NS on top, ERA5-*u* on bottom).

NS (synthetic). **ReMD** attains the best overall scores, surpassing image SR models (EDSR, SwinIR), neural operators (FNO, MWT, HiNOTE), and diffusion baselines (SR3, ResShift). Notably, even *ReMD-2* (two reverse steps) rivals or exceeds stronger baselines, while *ReMD-5* gives a small additional gain. The error maps in Fig. 1 (top) show sharper filaments and reduced small-scale errors compared to ResShift (15 steps) and non-diffusion SR, supporting our design of few-step, multiscale residual correction.

ERA5 (reanalysis). On realistic reanalysis fields, **ReMD** matches or improves upon the strongest image SR baselines in perceptual fidelity (PSNR/SSIM) while *also* lowering RMSE. The qualitative example (Fig. 1, bottom) highlights cleaner jets/fronts and fewer artifacts in the error maps. Neural-operator baselines degrade more noticeably on this dataset, whereas ReMD maintains spectral fidelity

and coherence—evidence that time-gated multigrid correction plus lightweight physics cues transfers beyond synthetic flows.

OCEAN (reanalysis). **ReMD** delivers the lowest numerical error and top or tied perceptual metrics. Competing methods either oversmooth mesoscale structures or introduce high-frequency noise, while ReMD preserves coherent, fine-scale patterns without sacrificing coarse-scale consistency, aligning with our operator view and restriction-based residual.

Summary. Across all three benchmarks, **ReMD** consistently improves RMSE while achieving state-of-the-art or tied PSNR/SSIM—with only 2–5 reverse steps, versus 15 for a strong diffusion baseline. These results support our motivation and design: (i) treating SR as iterative *residual* correction anchored by restriction consistency, and (ii) using a *time-gated multigrid* corrector to remove large-scale bias early and refine high-frequency structure later.

4.3. Model Analysis

4.3.1. Frequency-Domain Behaviour

We examine the radial error-energy spectrum on ERA5 (Fig. 3) to understand behaviour beyond pixel metrics. The two vertical dashed lines mark (i) the LR Nyquist band where large-scale flow energy concentrates, and (ii) the transition to very high wavenumbers near the HR Nyquist.

Large scales (left of first dash). ReMD exhibits the lowest error among all methods, indicating that its coarse-to-fine residual correction reduces large-scale bias rather than merely sharpening textures. Other methods show noticeably larger low-frequency errors, consistent with the visual mismatch of broad structures in Fig. 1.

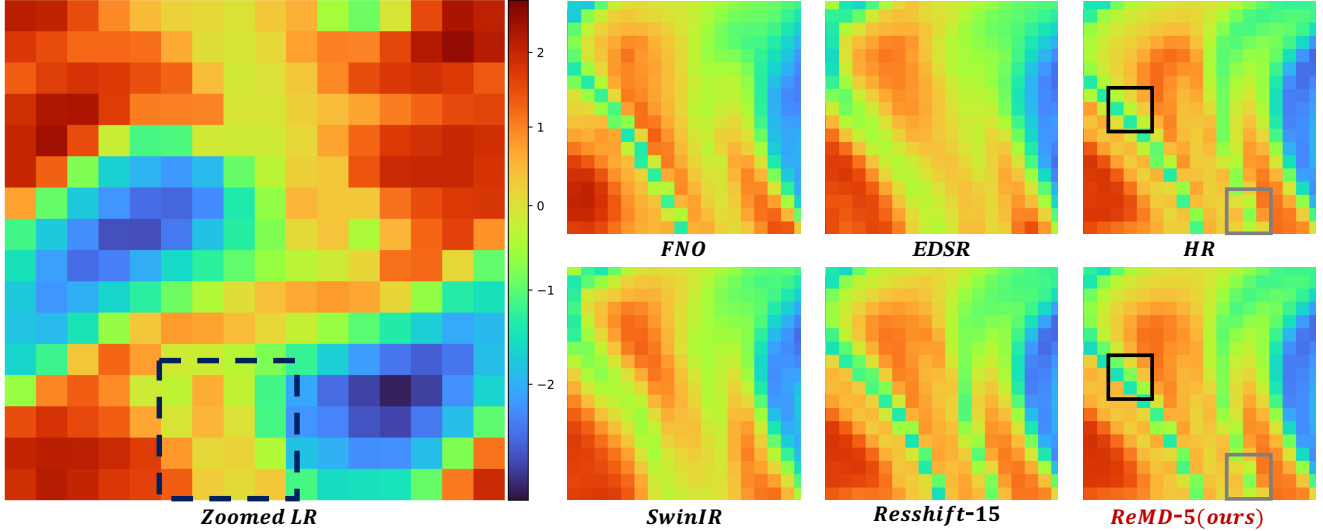


Figure 4. **Patch-level comparison on NS ($\times 4$).** Left: zoomed LR input. Black boxes highlight frontal bands; gray boxes mark small eddies. **ReMD-5** recovers sharper, HR-like fronts and coherent vortices with fewer steps than ResShift-15, while avoiding texture/aliasing artifacts seen in image-SR baselines and blockiness in FNO, and remaining consistent with the LR content.

Mid scales (between dashes). This band requires synthesizing subgrid content not present in the LR input. ReMD maintains a uniformly lower curve, reflecting the effect of the time-gated multigrid corrector that removes remaining smooth errors on coarse levels and progressively refines fronts/filaments on finer levels.

High scales (right of second dash). Near the HR Nyquist, ReMD keeps the error one to two orders lower than baselines, whereas SwinIR remains elevated and EDSR shows a late spike (ringing/aliasing). The spectrum-faithful tail aligns with our physics-consistent residuals and fixed multiwavelet transfers, which avoid hallucinated high-frequency textures.

Summary. Across scales, ReMD delivers the most spectrally faithful reconstructions, explaining its gains in metrics and the cleaner error maps shown in Fig. 1.

4.3.2. Patch-level spatial analysis

Fig. 4 contrasts a zoomed LR input with HR and baselines (FNO, EDSR, SwinIR, ResShift-15) versus **ReMD-5**. Key observations:

- **Front coherence.** Along the oblique front (black boxes), **ReMD** preserves sharp cross-front gradients and smooth along-front variation, closely matching HR; EDSR/SwinIR oversmooth and FNO staircases. ResShift-15 sharpens but shows haloing/misalignment.
- **Fine-scale eddy.** In the corner eddy (gray box), **ReMD** recovers a compact, coherent vortex; image SR baselines smear or hallucinate textures, and ResShift-15 exhibits a softened core with ringing.

Table 2. **Ablation study (OCEAN, $4\times$ SR).** Removing the MG corrector (“w/o residual correction”) or any physics residual (smoothing, anisotropic diffusion, spectrum) degrades all metrics; dropping the spectrum term yields the largest deterioration.

| MODEL CONFIGURATION | RMSE \downarrow | PSNR \uparrow | SSIM \uparrow |
|-------------------------|-------------------|-----------------|-----------------|
| W/O RESIDUAL CORRECTION | 1.38E-02 | 47.37 | 0.981 |
| W/O SMOOTHING RESIDUAL | 1.40E-02 | 47.28 | 0.981 |
| W/O DIFFUSION RESIDUAL | 1.40E-02 | 47.26 | 0.981 |
| W/O SPECTRUM RESIDUAL | 1.41E-02 | 47.20 | 0.981 |
| REMD (BASELINE) | 1.33E-02 | 47.71 | 0.983 |

- **Artifacts & consistency.** Inside the dashed LR patch, **ReMD** refines details without checkerboard/ripples, while FNO/SwinIR show aliasing and EDSR banding—consistent with multigrid residual correction (Sec. 3.2) and lightweight physics cues (Sec. 3.3).

Summary. **ReMD-5** attains HR-like fronts and small eddies with fewer steps than ResShift-15, aligning with its spectral and RMSE gains.

4.3.3. Ablation on multiscale correction and physics cues

As summarized in Table 2, removing any component degrades accuracy, with the multigrid corrector providing the main reduction of large-scale bias and the spectrum term contributing the largest share of high-frequency fidelity among the physics cues; smoothness and anisotropic diffusion act as stabilizers that suppress artifacts and preserve fronts. Overall, these parts are complementary—together they enable few-step sampling with the best performance.

Table 3. **Efficiency on the NS.** We report accuracy (RMSE↓/PSNR↑), parameter size, and wall-time (training time per epoch; inference time in seconds). Diffusion baselines (SR3, ResShift-15) incur high sampling cost; **ReMD-5** attains the best accuracy with fewer steps and lower inference time than ResShift, while **ReMD-2** is the fastest with competitive accuracy.

| METRICS | METHODS | | | | | | | | | |
|--------------------------|----------|----------|----------|----------|----------|----------|----------|-----------|-----------|----------|
| | EDSR | FNO | MWT | HiNOTE | GALERKIN | SWINIR | SR3 | RESSHIFT | REMD-2 | REMD-5 |
| RMSE ↓ | 2.97E-02 | 4.42E-02 | 8.45E-02 | 8.03E-02 | 5.32E-02 | 3.63E-02 | 3.34E-01 | 2.21E-02 | 2.11E-02 | 2.09E-02 |
| PSNR ↑ | 46.89 | 43.44 | 37.81 | 38.25 | 41.83 | 45.15 | 25.87 | 49.47 | 49.84 | 49.94 |
| PARAM COUNT | 1367553 | 684065 | 272605 | 420618 | 703777 | 3696633 | 93868033 | 112366821 | 118584941 | |
| PARAM(MB) | 5.22 | 5.17 | 1.75 | 1.61 | 2.68 | 17.85 | 358.17 | 428.65 | 455.55 | |
| TRAINING TIME (S/EPOCH) | 8.87 | 4.78 | 1.72 | 57.91 | 146.25 | 86.26 | 53.48 | 64.1 | 100.33 | |
| INFERENCE TIME (S/EPOCH) | 0.05 | 0.03 | 0.05 | 0.75 | 0.62 | 0.32 | 697.64 | 8.07 | 2.33 | 5.84 |

Table 4. **Physics-related metrics (lower is better ↓).** VE/EE are vorticity/enstrophy errors on NS2D ($\times 4$). GED is the energy discrepancy on ERA5_uo ($\times 4$). The last column reports RMSE on ERA5_uo $\times 8$ super-resolution.

| Model | VE ↓ | EE ↓ | GED ↓ | RMSE ($\times 8$) ↓ |
|--------------------|-----------------|-----------------|-----------------|-----------------------|
| FNO | 5.01E-03 | 2.57E-05 | 5.45E-02 | 3.76E-01 |
| EDSR | 6.43E-03 | 9.41E-05 | 4.38E-03 | 3.39E-01 |
| SwinIR | 6.16E-03 | 6.86E-05 | 5.10E-03 | 3.34E-01 |
| LIIF | 4.99E-03 | 2.08E-05 | 6.14E-03 | 3.32E-01 |
| ResShift | 3.26E-03 | 1.11E-05 | 4.51E-03 | 3.49E-01 |
| ReMD (ours) | 2.34E-03 | 3.56E-06 | 4.24E-03 | 3.23E-01 |

4.3.4. Efficiency

Compared with diffusion baselines (Table 3), **ReMD** is markedly more *inference-efficient* at the same or better accuracy. SR3 requires very long sampling (hundreds of steps), leading to orders-of-magnitude slower inference and much worse accuracy. ResShift shortens sampling to 15 steps and improves quality, but still trails ReMD both in error and speed. With only 5 steps, **ReMD-5** attains the best RMSE/PSNR while running $\sim 1.4\times$ faster than ResShift; with 2 steps, **ReMD-2** remains more accurate than ResShift and is $\sim 3.5\times$ faster.

The gains stem from treating each reverse step as a multi-grid residual correction: fixed multiwavelet transfers and depthwise smoothers keep per-step cost $\mathcal{O}(HW)$ with a small constant, so wall-time scales primarily with the *number of steps*. Although ReMD carries a slightly larger parameter footprint and higher per-epoch *training* time (due to time-gated multiscale passes), inference is the dominant cost at deployment; on this Pareto front (error vs. time), ReMD strictly dominates both SR3 and ResShift.

5. Conclusion

We presented **ReMD**, a physics-consistent diffusion framework that treats fluid SR as iterative residual correction. By coupling restriction consistency with lightweight physics cues and a time-gated multigrid corrector built on fixed multiwavelet transfers, ReMD attains state-of-the-art accuracy on NS, ERA5, and Ocean benchmarks with only

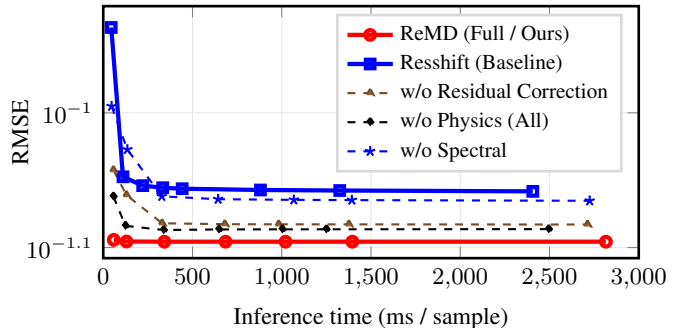


Figure 5. **Time-RMSE trade-off on ERA5_uo ($\times 4$ SR).** Each point varies the sampling steps; lower-left is better.

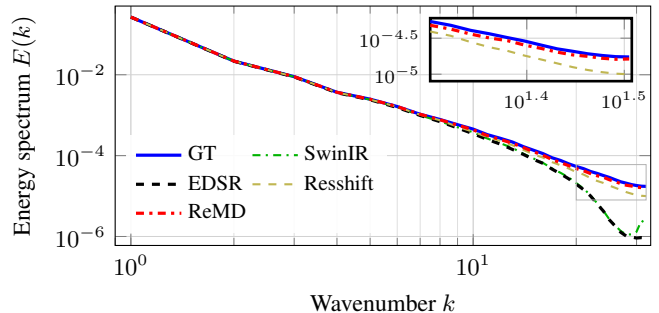


Figure 6. NS2D energy spectrum (log-log).

2–5 reverse steps, and produces spectrally faithful, low-divergence reconstructions.

Limitations & future directions. (i) *Pixel-space scaling.* Operating in pixel space constrains memory and compute at very high target resolutions; moving ReMD to latent domains can decouple cost from HR grid size and enable higher-resolution SR. (ii) *Mid-band accuracy.* Mid-frequency errors are reduced less effectively than low or high bands; introducing band-pass residuals, per-band (timestep-conditioned) gating, and refined spectrum-aware losses can better target the intermediate wavenumbers. (iii) *Temporal rollout.* Current evaluation is single-frame; integrating ReMD as a corrector in forecasting (predictor-corrector with neural operators), assessing long-horizon stability, and adding lightweight physics consistent projections during rollout address this gap.

References

- [1] Johannes Brandstetter, Daniel Worrall, and Max Welling. Message passing neural pde solvers. *arXiv preprint arXiv:2202.03376*, 2022. 1
- [2] W.L. Briggs, V.E. Henson, and S.F. McCormick. *A Multigrid Tutorial, second ed.* SIAM, California, 2000. 1, 3
- [3] Shuhao Cao. Choose a transformer: Fourier or galerkin. *Advances in neural information processing systems*, 34:24924–24940, 2021. 6
- [4] E.U. Copernicus Marine Service Information (CMEMS). Global Ocean Physics Reanalysis. Marine Data Store (MDS), 2023. 5
- [5] Gaurav Gupta, Xiongye Xiao, and Paul Bogdan. Multiwavelet-based operator learning for differential equations. *Advances in neural information processing systems*, 34:24048–24062, 2021. 6
- [6] Juncai He, Xinliang Liu, and Jinchao Xu. Mgno: Efficient parameterization of linear operators via multigrid. In *ICLR*. OpenReview.net, 2024. 1
- [7] Hans Hersbach, Bill Bell, Paul Berrisford, Gionata Biavati, András Horányi, Joaquín Muñoz Sabater, Julien Nicolas, Carole Peubey, Raluca Radu, Iryna Rozum, Dick Schepers, Adrian Simmons, Côme Soci, Dick Dee, and Jean-Noël Thépaut. ERA5 hourly data on pressure levels from 1940 to present. Copernicus Climate Change Service (C3S) Climate Data Store (CDS), 2023. Accessed on 04-Oct-2025. 5
- [8] Diederik P. Kingma and Jimmy Ba. Adam: A method for stochastic optimization. In *ICLR (Poster)*, 2015. 5
- [9] Dmitrii Kochkov, Jamie A Smith, Ayya Alieva, Qing Wang, Michael P Brenner, and Stephan Hoyer. Machine learning–accelerated computational fluid dynamics. *Proceedings of the National Academy of Sciences*, 118(21):e2101784118, 2021. 1
- [10] Nikola Kovachki, Zongyi Li, Burigede Liu, Kamyar Azizzadenesheli, Kaushik Bhattacharya, Andrew Stuart, and Anima Anandkumar. Neural operator: Learning maps between function spaces with applications to pdes. *Journal of Machine Learning Research*, 24(89):1–97, 2023. 1
- [11] Bessy M Kuriakose et al. Edsr: Empowering super-resolution algorithms with high-quality div2k images. *Intelligent Decision Technologies*, 17(4):1249–1263, 2023. 5
- [12] Zongyi Li, Nikola Kovachki, Kamyar Azizzadenesheli, Burigede Liu, Kaushik Bhattacharya, Andrew Stuart, and Anima Anandkumar. Fourier neural operator for parametric partial differential equations. *arXiv preprint arXiv:2010.08895*, 2020. 1, 6
- [13] Zhihao Li, Zhilu Lai, Xiaobo Zhang, and Wei Wang. M2no: Multiresolution operator learning with multiwavelet-based algebraic multigrid method. 2024. 1, 4
- [14] Jingyun Liang, Jiezhong Cao, Guolei Sun, Kai Zhang, Luc Van Gool, and Radu Timofte. Swinir: Image restoration using swin transformer. In *Proceedings of the IEEE/CVF international conference on computer vision*, pages 1833–1844, 2021. 6
- [15] Xihai Luo, Xiaoning Qian, and Byung-Jun Yoon. Hierarchical neural operator transformer with learnable frequency-aware loss prior for arbitrary-scale super-resolution. *arXiv preprint arXiv:2405.12202*, 2024. 6
- [16] Adam Paszke, Sam Gross, Francisco Massa, Adam Lerer, James Bradbury, Gregory Chanan, Trevor Killeen, Zeming Lin, Natalia Gimelshein, Luca Antiga, et al. Pytorch: An imperative style, high-performance deep learning library. *Advances in neural information processing systems*, 32, 2019. 5
- [17] Stephan Rasp, Michael S Pritchard, and Pierre Gentine. Deep learning to represent subgrid processes in climate models. *Proceedings of the national academy of sciences*, 115(39):9684–9689, 2018. 1
- [18] Robin Rombach, Andreas Blattmann, Dominik Lorenz, Patrick Esser, and Björn Ommer. High-resolution image synthesis with latent diffusion models. In *Proceedings of the IEEE/CVF conference on computer vision and pattern recognition*, pages 10684–10695, 2022. 1
- [19] Chitwan Saharia, Jonathan Ho, William Chan, Tim Salimans, David J Fleet, and Mohammad Norouzi. Image super-resolution via iterative refinement. *IEEE transactions on pattern analysis and machine intelligence*, 45(4):4713–4726, 2022. 1
- [20] Karen Stengel, Andrew Glaws, Dylan Hettinger, and Ryan N King. Adversarial super-resolution of climatological wind and solar data. *Proceedings of the National Academy of Sciences*, 117(29):16805–16815, 2020. 1
- [21] Makoto Takamoto, Timothy Praditia, Raphael Leiteritz, Daniel MacKinlay, Francesco Alesiani, Dirk Pflüger, and Mathias Niepert. Pdebench: An extensive benchmark for scientific machine learning. *Advances in Neural Information Processing Systems*, 35:1596–1611, 2022. 5
- [22] Xintao Wang, Liangbin Xie, Chao Dong, and Ying Shan. Real-esrgan: Training real-world blind super-resolution with pure synthetic data. In *Proceedings of the IEEE/CVF international conference on computer vision*, pages 1905–1914, 2021. 5
- [23] Zhihao Wang, Jian Chen, and Steven CH Hoi. Deep learning for image super-resolution: A survey. *IEEE transactions on pattern analysis and machine intelligence*, 43(10):3365–3387, 2020. 1
- [24] Jinchao Xu and Ludmil T. Zikatanov. The method of alternating projections and the method of subspace corrections in hilbert space. *Journal of the American Mathematical Society*, 15:573–597, 2002. 3
- [25] Zongsheng Yue, Jianyi Wang, and Chen Change Loy. Resshift: Efficient diffusion model for image super-resolution by residual shifting. *Advances in Neural Information Processing Systems*, 36:13294–13307, 2023. 2, 5
- [26] Peng Zheng, Travis Askham, Steven L Brunton, J Nathan Kutz, and Aleksandr Y Aravkin. A unified framework for sparse relaxed regularized regression: Sr3. *IEEE Access*, 7: 1404–1423, 2018. 5